九州大学学術情報リポジトリ
Kyushu University Institutional Repository

Relativisitic particle acceleration in developing Alfve´n turbulence

Matsukiyo, Shuichi
Department of Earth System Science and Technology, Kyushu University

Hada, Tohru
Department of Earth System Science and Technology, Kyushu University

https://hdl.handle.net/2324/16869

出版情報：The Astrophysical Journal. 692 (2), pp.1004-1012, 2009-02-23. AAS
バージョン：
権利関係：

KYUSHU UNIVERSITY

The Astrophysical Journal, 692:1004–1012, 2009 February 20 doi:10.1088/0004-637X/692/2/1004
© 2009. The American Astronomical Society. All rights reserved. Printed in the U.S.A.

RELATIVISTIC PARTICLE ACCELERATION IN DEVELOPING ALFVÉN TURBULENCE

S. Matsukiyo and T. Hada
Department of Earth System Science and Technology, Kyushu University, 6-1 Kasuga-Koen, Kasuga, 816-8580, Fukuoka, Japan; matsukiy@esst.kyushu-u.ac.jp
Received 2008 June 9; accepted 2008 October 21; published 2009 February 23

ABSTRACT

A new particle acceleration process in a developing Alfvén turbulence in the course of successive parametric instabilities of a relativistic pair plasma is investigated by utilizing one-dimensional electromagnetic full particle code. Coherent wave–particle interactions result in efficient particle acceleration leading to a power-law-like energy distribution function. In the simulation, high-energy particles having large relativistic masses are preferentially accelerated as the turbulence spectrum evolves in time. The main acceleration mechanism is simultaneous relativistic resonance between a particle and two different waves. An analytical expression of maximum attainable energy in such wave–particle interactions is derived.

Key words: acceleration of particles – cosmic rays – plasmas – relativity – turbulence – waves

Online-only material: color figures

1. INTRODUCTION

Large amplitude Alfvén waves are ubiquitous in space and astrophysical environments. Such waves are believed to play key roles in the so-called diffusive shock acceleration (DSA) process in which charged particles are diffusively accelerated in the course of multiple scattering through turbulent Alfvén waves upstream and downstream of collisionless shocks. The DSA is widely accepted as one of the most efficient acceleration mechanisms of galactic cosmic rays of energy up to $\sim 10^{15.5}$ eV (Krymsky 1977; Axford et al. 1977; Bell 1978; Blandford & Ostriker 1978; Drury 1983; Lagage & Cesarsky 1983; Blandford & Eichler 1987; Jones & Ellison 1991; Malkov & Drury 2001; Duffy & Blundell 2005). In the process, it is implicitly assumed that the Alfvén turbulence is phase randomized and its spectrum is time stationary. On the other hand, turbulent Alfvén waves commonly observed in the solar–terrestrial environments are often intermittent, and coherent MHD structures are frequently superposed. Namely, the phase random approximation cannot be assumed (de Wit et al. 1999; Hada et al. 2003; Narita et al. 2006) and a spectrum of turbulence may evolve both in space and time (Bruno & Carbone 2005). This is probably due to the fact that nonlinear wave–wave interactions tend to generate coherence among wave phases, and that spatial and temporal scales of relaxation processes in space plasmas are much larger than typical scales of our solar–terrestrial system. This may hold true with some high-energy astrophysical environments. That is, spatial and temporal scales of a relaxation process are not negligibly small in comparison with scales of a whole acceleration site. Generally speaking, particle acceleration rate through coherent wave–particle interactions is much higher than that through incoherent, or fully turbulent, wave–particle interactions (Kuramitsu & Hada 2000, 2008). Therefore, acceleration processes through coherent wave–particle interactions in a ‘developing’ turbulence, where a turbulence has not been fully developed, should be paid more serious attention.

It is well known that in various space plasma environments, a nonequilibrium ion distribution function generates large-amplitude Alfvén waves through some instabilities and that those waves nonlinearly evolve to produce coherent magnetic wave forms. One of the common interpretations of generation mechanisms of such wave forms accompanying density fluctuations which are frequently observed in the solar wind (Spangler et al. 1997; Spangler & Fuselier 1988) is a parametric instability where nonlinear wave–wave interactions convert the energy of a parent wave into several daughter waves with different frequencies and wavelengths (Galeev & Oraevskii 1963; Sagdeev & Galeev 1969). Although in the context of cosmic ray acceleration in turbulent media the above process was taken into account to estimate steady state distributions of wave intensities (Chin & Wentzel 1972; Wentzel 1974; Skilling 1975a, 1975b, 1975c), its developing processes and associated coherent wave–particle interactions have never been considered. Recent numerical studies revealed that successive parametric instabilities result in turbulent wave forms, which have not been fully developed (Matsukiyo & Hada 2003; Nariyuki & Hada 2005, 2006). However, only a few past studies paid much attention to particle acceleration processes in such a developing turbulence. Furthermore, only limited spatial and temporal evolutions of wave forms or spectra were discussed, since a computational resource was limited.

In this paper, long time evolution of parametric instabilities of a large amplitude Alfvén wave in a rather large spatial domain is reproduced by utilizing one-dimensional relativistic full particle-in-cell (PIC) code. A plasma is assumed to be composed of electrons and positrons, since electron–positron pairs can be the dominant constituent of some high-energy astrophysical plasmas such as in the vicinity of a pulsar, active galactic nucleus (AGN), gamma ray burst (GRB), and so on. In the simulation, we observe a particle acceleration process which is quite efficient and is due to interactions between coherent Alfvén waves and relativistic particles. The process is quite different from some other coherent acceleration processes being discussed recently, in which high-frequency electrostatic waves play essential roles, such as electron surfing acceleration induced by a cross-field Buneman instability (Shimada & Hoshino 2000; McClements et al. 2001; Hoshino & Shimada 2002; Dieckmann et al. 2004, 2005; Amano & Hoshino 2007) and wake field acceleration (Tajima & Dawson 1979; Katsouleas & Dawson 1983; Lyubarsky 2006; Hoshino 2008).

Simulation settings and results are represented in Section 2. The acceleration process is discussed in detail by using an analytical model and test particle simulation in Section 3. Summary and discussions are given in Section 4.

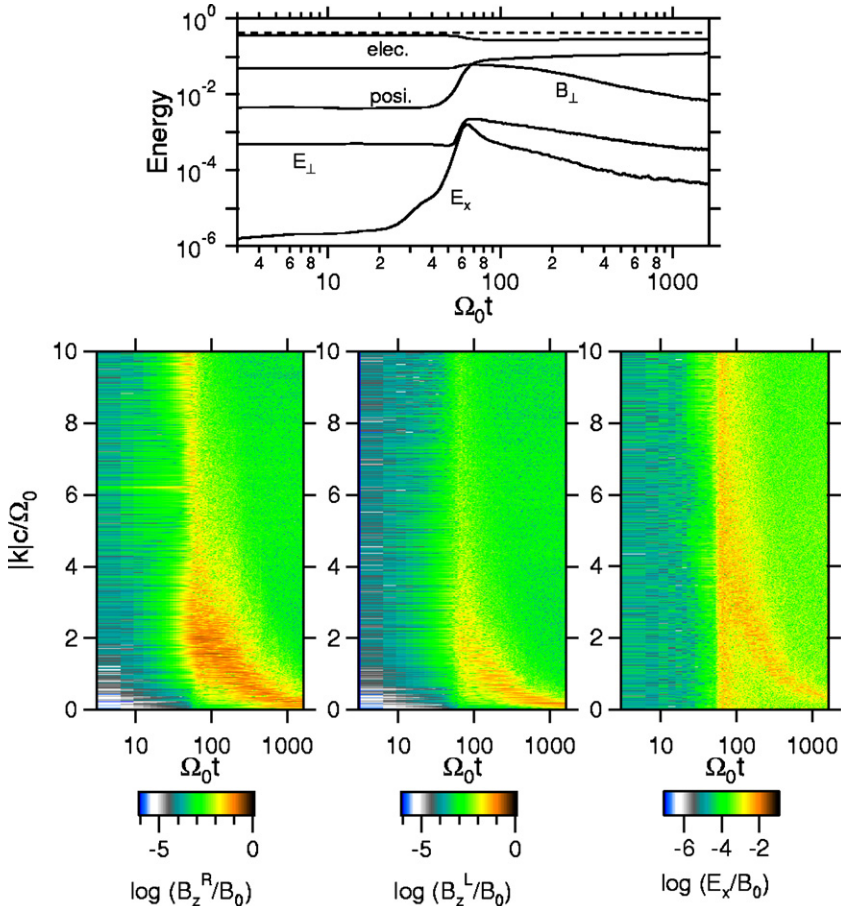

Figure 1. Energy time history (upper panel) and time evolution of wave power spectra (lower panel). In the lower panel the right- and left-hand helicity modes of the B_z component are Fourier decomposed in the left and middle panels, respectively. The right panel shows the E_x component.

(A color version of this figure is available in the online journal.)

2. 1D PIC SIMULATION

Long time evolution of parametric instabilities of a large-amplitude monochromatic Alfvén wave in a relativistic pair plasma is reproduced by performing a one-dimensional PIC simulation. A parent wave is given only at the beginning of the run as a monochromatic and right-handed circularly polarized Alfvén wave with amplitude $B_p/B_0 = 1$ and wavenumber $k_0 c/\Omega_0 = 6.21$ (number of wave mode is 512) which gives a frequency $\omega_0/\Omega_0 = 0.627$, where $\mathbf{B_0}$ is the ambient magnetic field which is along the x-axis, c denotes the speed of light, and $\Omega_0 = eB_0/m_0 c$ is the nonrelativistic gyro frequency, respectively. Corresponding velocity perturbations of the pair plasma are given by the relativistic Walen relation (Hada et al. 2004). Boundary conditions are periodic for particles and all field components. The system size is $L = 518.1c/\Omega_0$. The squared ratio of nonrelativistic gyro and plasma frequencies is $\Omega_0^2/\omega_p^2 = 0.1$, and the normalized scalar temperature for both electrons and positrons is $T/m_0c^2 = 1.6 \times 10^{-3}$.

Figure 1 shows time evolutions of energy densities (upper panel) and Fourier spectra of wave amplitudes for B_z and E_x field components (lower panels). In the upper panel, the solid lines denote electron and positron kinetic energies (labeled by “elec.” and “posi.”), transverse magnetic field energy (“$B_\perp$”), and transverse and longitudinal electric field energies (“$E_\perp$” and “E_x”), respectively. The dashed line indicates the total energy, which is well conserved during the run. Although a rather long system evolution (up to $\Omega_0 t = 1616$) is calculated, the system is still far from the so-called equilibrium state. In the lower panels, wave amplitude spectra for positive and negative helicity (corresponding to positive and negative wavenumbers, respectively) modes of the B_z component are shown in the left (B_z^R) and middle (B_z^L) panels by using a technique of Fourier decomposition (Terasawa et al. 1986). Note that in the middle panel, the actual sign of the wavenumber is negative. Since most of the daughter waves are right-hand polarized, the left (middle) panel shows wave intensity mainly of positively (negatively) propagating waves. At the beginning, only the parent wave has significant intensity at $kc/\Omega_0 = 6.21$ in the left panel, although it is not particularly outstanding in the figure because of the narrow spectrum. In the early stage, $50 < \Omega_0 t < 100$, the parent wave energy is transferred to a variety of daughter waves through large number of channels of wave–wave interactions. In this stage, two parametric instabilities are dominant. A modulational instability generates daughter magnetic fluctuations with the same signs of wavenumber as that of the parent wave. They are observed in the B_z^R spectrum. Couplings among the daughter and the parent waves result in compressional electrostatic fluctuations with a wavenumber smaller than that of the parent wave as seen in the right panel. In a decay instability, on the other hand, daughter magnetic fluctuations have negative wavenumbers which appear in the B_Z^L spectrum, while daughter electrostatic fluctuations have wavenumbers larger than that of the parent wave in the right panel. Most of the parent wave energy is wasted in this stage. However, the intensities of the daughter waves are still large so that successive parametric

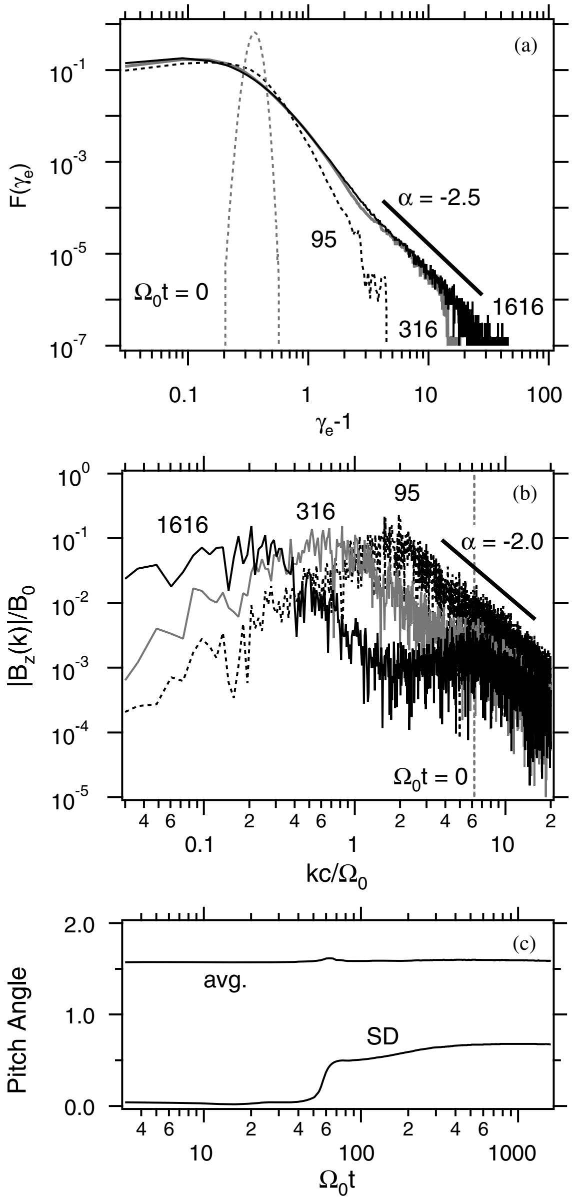

Figure 2. (*a*) Electron energy distribution functions (upper panel) and (*b*) Fourier amplitude spectra of the B_z component (middle panel) at various times. (*c*) Time evolution of an average pitch angle of electrons and its standard deviation.

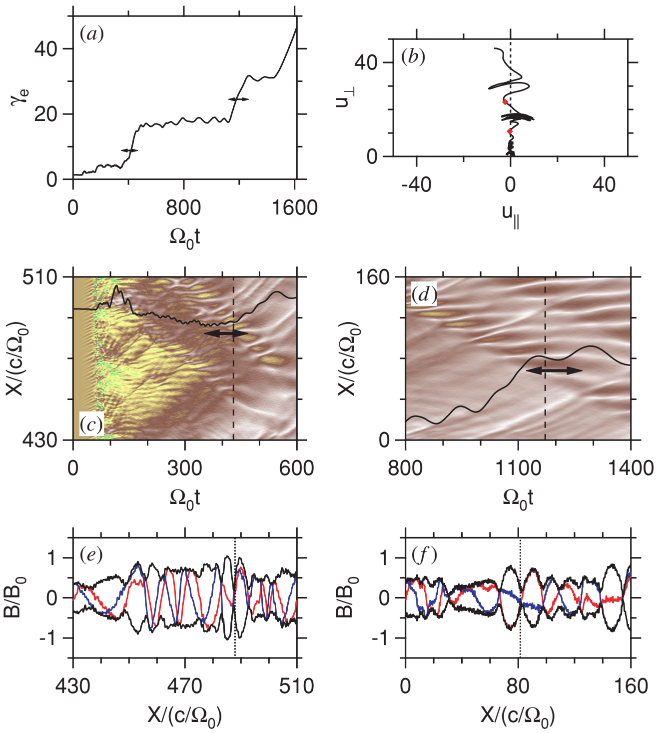

Figure 3. Behaviors of an accelerated electron. (*a*) Time history of the electron energy. (*b*) Trajectories of the electron in $u_\perp - u_\parallel$ space and (*c*, *d*) in the $X-t$ space. The arrows in (*c*) and (*d*) indicate time domains where strong acceleration occurs as shown by the arrows in (*a*). Background color scale in (*c*) and (*d*) denotes amplitude of magnetic fluctuations. (*e*, *f*) Spatial profiles of magnetic fluctuations in two acceleration phases represented by dashed lines in (*c*) and (*d*). The red, blue, and black solid lines show B_y, B_z components, and envelope, respectively. The dotted lines show positions of the particle at corresponding times.

(A color version of this figure is available in the online journal.)

instabilities occur thereafter. These successive processes are sustained mainly by decay instabilities which can be confirmed because peak wavenumbers of the E_x spectrum is always larger than those of the B_z^R and B_z^L spectra. The previous simulation study by Matsukiyo & Hada (2003) confirmed the occurrence of up to the second decay instability for the case of $B_p/B_0 = 0.1$.

Figure 2(a) demonstrates electron energy distribution functions at various times. Fourier amplitude spectra of the B_z component at the corresponding times are plotted in Figure 2(b). Rapid heating occurs after the first instabilities developed ($\Omega_0 t = 95$; black dashed line). Up to this stage, most of the electrons show semistochastic motions in a noisy system with a primary wave. Here we refer the primary wave and the noise to the parent wave and superposition of the daughter waves, respectively. This results in rapid scattering in pitch angle as shown in Figure 2(c), where an average pitch angle of electrons with respect to $\mathbf{B_0}$ and its standard deviation are plotted as a function of time. The standard deviation just after its rapid growth at $\Omega_0 t \sim 70$ is ~ 0.5, which roughly coincides with an analytical estimate of the maximum pitch angle width of an electron resonating with the monochromatic parent wave (see the Appendix). After the parent wave disappears, most of the electrons are detrapped by the parent wave and start to wander in the phase space. As time passes, a high-energy tail appears in the electron distribution function (Figure 2(a)), which gradually approaches a power-law spectrum with index $\alpha \sim -2.5$ ($\Omega_0 t = 316$: gray solid line, 1616: black solid line). At the same time, the wave amplitude spectrum develops the power-law-type spectrum also, with the index $\alpha \sim -2.0$, while the wave spectral peak shifts toward lower wavenumbers.

A behavior of the most efficiently accelerated electron is shown in Figure 3. Figure 3(a) indicates the energy time history of the electron. Spatial trajectory of the electron during $0 < \Omega_0 t < 600$ ($800 < \Omega_0 t < 1400$) is plotted in Figures 3(c) and (d). A background color scale denotes the strength of magnetic fluctuations $B_\perp \equiv \sqrt{B_y^2 + B_z^2}$. The horizontal arrows in Figures 3(c), (d), and (a) correspond to each other denoting time intervals where strong accelerations occur. Figures 3(e) and (f) show a snapshot of the wave profile at the time denoted as the dashed line in Figures 3(c) and (d). The red, blue, and black lines represent B_y, B_z, and an envelope, respectively. The dotted line indicates the position of the electron. It is seen that strong acceleration occurs when the electron is trapped in a trough of the magnetic envelope. Such sharp envelope troughs are temporarily observed in various regions of the system throughout the run. Hence, the electron experiences similar acceleration processes several times. In this example, one may recognize four such acceleration periods. Only the second and the third periods are marked (the first (fourth) one is $160 < \Omega_0 t < 190$ ($\Omega_0 t > 1450$)). The acceleration occurs always perpendicular to $\mathbf{B_0}$ as seen in Figure 3(b) which shows a trajectory of the electron in the $u_\perp - u_\parallel$ space, where $u_\perp$ and $u_\parallel$ denote the four-velocities perpendicular and parallel to $\mathbf{B_0}$. The red markers indicate positions of the electron in the phase space at the same time as Figures 3(e) (lower marker) and 3(f) (upper marker). We checked a hundred most efficiently accelerated electrons' trajectories and confirmed that all of them show essentially the same features as mentioned above, i.e., trapping within the envelope troughs and successive perpendicular acceleration. In the next section, the acceleration process is modeled and analyzed in detail.

3. ACCELERATION OF HIGH-ENERGY ELECTRONS

3.1. Coherent Waves Observed in the Simulation: Modeling

In the PIC simulation shown above, sharp magnetic envelope troughs are locally formed throughout the period of strong electron accelerations. In a successive decay process, a number of daughter Alfvén waves propagating both parallel and antiparallel to $\mathbf{B_0}$ are excited. Depending on their phases, amplitudes of some wave modes are sometimes locally cancelled out each other, or they are simply less dominant in amplitude. Then, there appear some regions where two oppositely propagating waves dominate. Here, the envelope structures observed in the PIC simulation are modeled by a superposition of such two oppositely propagating waves as follows.

$$\begin{pmatrix} B_w^y \\ B_w^z \end{pmatrix} = B_w \cos kx \begin{pmatrix} \cos \omega t \\ \sin \omega t \end{pmatrix} \tag{1}$$

$$\begin{pmatrix} E_w^y \\ E_w^z \end{pmatrix} = -\frac{\omega}{kc} B_w \sin kx \begin{pmatrix} \cos \omega t \\ \sin \omega t \end{pmatrix} \tag{2}$$

Equation (1) is equivalent to

$$\mathbf{B_w} = \frac{B_w}{2} \begin{pmatrix} \cos(kx - \omega t) \\ -\sin(kx - \omega t) \end{pmatrix} + \frac{B_w}{2} \begin{pmatrix} \cos(-kx - \omega t) \\ -\sin(-kx - \omega t) \end{pmatrix}.$$

Hereafter, we assume ω and k are both positive without losing generality. Typical waveforms at two different time domains are shown in Figures 4(a) and b. The black solid and dashed lines denote y and z components of rotating carrier waves, and the gray lines represent envelopes which is independent of time. In the neighborhood of a trough, it is confirmed that Equations (1) and (2) give a reasonable model of a waveform observed in the PIC simulation shown in Figure 4(c). In the following section, the motion of a test particle in this system is analyzed.

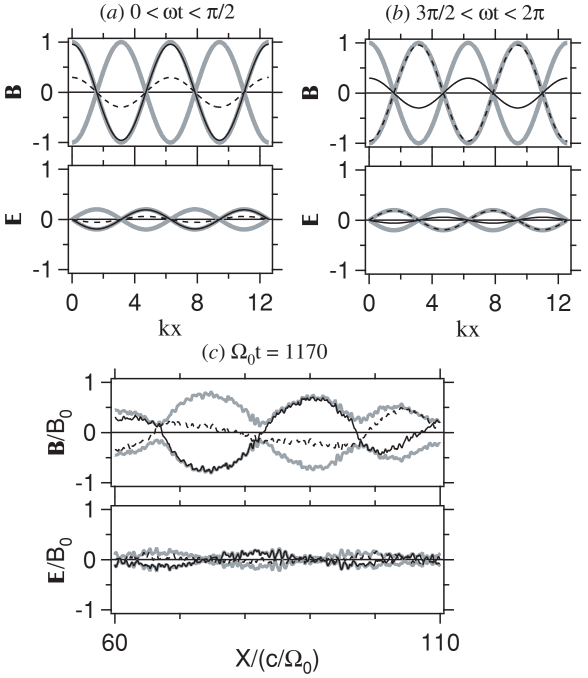

Figure 4. (a, b) Modeled wave forms at different time domains ($B_w = 1, \omega/kc = 0.2$), and (c) an example of a waveform seen in the PIC simulation at $\Omega_0 t = 1170$.

3.2. Motion of a Particle in Given EM Fields

In this section, we consider the motion of an electron in the electromagnetic waves given by Equations (1) and (2). The equation of motion is

$$\frac{d\mathbf{u}}{dt} = -\frac{e}{m_0 c}\left(\mathbf{E} + \frac{\mathbf{u}}{\gamma} \times \mathbf{B}\right), \tag{3}$$

$$\frac{dx}{dt} = \frac{u_x}{\gamma} c, \tag{4}$$

where $\mathbf{u} \equiv \gamma \mathbf{v}/c$, $\gamma = \sqrt{1 + u^2}$, e and m_0 indicate charge and rest mass of the electron, $\mathbf{B} = B_0 \mathbf{x} + \mathbf{B_w}$, and $\mathbf{E} = \mathbf{E_w}$, respectively. When we write $\mathbf{u} = (u_\parallel(t), u_\perp(t)\cos\phi(t), u_\perp(t)\sin\phi(t))$ and introduce normalized variables as $\xi = x\Omega_0/c$, $\tau = \Omega_0 t$, $\kappa = kc/\Omega_0$, $\nu = \omega/\Omega_0$, $b_w = B_w/B_0$, and $v_{\rm ph} = \nu/\kappa$, Equations (3) and (4) are written as follows.

$$\dot{u}_\parallel = b_w \frac{u_\perp}{\gamma} \cos\kappa\xi \sin\psi \tag{5}$$

$$\dot{u}_\perp = b_w \left(v_{\rm ph} \sin\kappa\xi \cos\psi - \frac{u_\parallel}{\gamma} \cos\kappa\xi \sin\psi \right) \tag{6}$$

$$\dot{\psi} = -\frac{b_w}{u_\perp}\left(v_{\rm ph} \sin\kappa\xi \sin\psi + \frac{u_\parallel}{\gamma}\cos\kappa\xi\cos\psi \right) - \left(\nu - \frac{1}{\gamma} \right) \tag{7}$$

$$\dot{\xi} = \frac{u_\parallel}{\gamma} \tag{8}$$

Here, $\psi = \phi - \nu\tau$, and the dot denotes time derivative in terms of τ, respectively. Note that a variation of normalized particle energy, or the Lorentz factor, is given as

$$\dot{\gamma} = b_w v_{\rm ph} \frac{u_\perp}{\gamma} \sin\kappa\xi \cos\psi. \tag{9}$$

In the following, behaviors of the electron is discussed by using Equations (5)–(9).

3.3. Fixed Point Analysis

The above set of equations clearly has several fixed points as listed in Table 1. Here, u_0 denotes a value of $u_\perp$ at a corresponding fixed point and $\gamma_0 = \sqrt{1 + u_0^2}$. Apparently, the fixed points I–III (IV–VI) correspond to troughs (crests) of the magnetic envelope. As far as the acceleration is concerned, it is easily inferred that the fixed points IV–VI are not important since

Table 1
Fixed Points

No.	$\kappa\xi$	ψ	$u_\parallel$	$u_\perp$	Constraint
I	$\pm\frac{\pi}{2}$	$\pm\frac{\pi}{2}$	0	$-\frac{b_w v_{\mathrm{ph}}}{u_0} = \left(\nu - \frac{1}{\gamma_0}\right)$	
II	$\pm\frac{\pi}{2}$	$\mp\frac{\pi}{2}$	0	$\frac{b_w v_{\mathrm{ph}}}{u_0} = \left(\nu - \frac{1}{\gamma_0}\right)$	
III	$\pm\frac{\pi}{2}$	$0(\pi)$	0	0	$\frac{\sin\psi}{u_0} \to \mp\left(\nu - \frac{1}{\gamma_0}\right)/b_w v_{\mathrm{ph}}$
IV	$0(\pi)$	$0(\pi)$	0	$\nu - \frac{1}{\gamma_0} = 0$	
V	$0(\pi)$	$\pi(0)$	0	$\nu - \frac{1}{\gamma_0} = 0$	
VI	$0(\pi)$	$\pm\frac{\pi}{2}$	0	0	$\frac{\sin\kappa\xi}{u_0} \to \mp\left(\nu - \frac{1}{\gamma_0}\right)/b_w v_{\mathrm{ph}}$

the electric field strength is very weak around there. Actually, efficient acceleration observed in the PIC simulation always occurs around the troughs of the magnetic envelope. Therefore, only the fixed points I–III are focused here. Stability of these fixed points is discussed in the following.

3.3.1. Stability of the Fixed Points I–III

Expanding Equations (5)–(9) around the fixed point I and retaining only the first-order terms, we obtain

$$\delta\dot{u}_\parallel = -b_w \frac{u_0}{\gamma_0}\kappa\delta\xi, \tag{10}$$

$$\delta\dot{u}_\perp = -b_w v_{\mathrm{ph}}\delta\psi, \tag{11}$$

$$\delta\dot{\psi} = \frac{b_w}{u_0^2} v_{\mathrm{ph}}\delta u_\perp - \frac{1}{\gamma_0^2}\delta\gamma, \tag{12}$$

$$\delta\dot{\xi} = \frac{\delta u_\parallel}{\gamma_0} \tag{13}$$

$$\delta\dot{\gamma} = -b_w \frac{u_0}{\gamma_0} v_{\mathrm{ph}}\delta\psi = \frac{u_0}{\gamma_0}\delta\dot{u}_\perp, \tag{14}$$

where δ denotes small first-order quantities.

From Equations (10) and (13), we have

$$\delta\ddot{u}_\parallel = -b_w \frac{u_0}{\gamma_0^2}\kappa\delta u_\parallel. \tag{15}$$

The above expression represents a trapping oscillation with trapping frequency $\omega_{\mathrm{trap}} = \left(b_w u_0 \kappa/\gamma_0^2\right)^{1/2}$, which is rewritten with the original parameters as $\omega_{\mathrm{trap}} = (B_w k c u_0/B_0\Omega_0\gamma_0^2)^{1/2}$.

From Equations (11), (12), and (14), on the other hand, we obtain

$$\delta\ddot{u}_\perp = \frac{b_w u_0 v_{\mathrm{ph}}}{\gamma_0^3}\left(1 - b_w v_{\mathrm{ph}}\frac{\gamma_0^3}{u_0^3}\right)\delta u_\perp. \tag{16}$$

Here, the first term in the parenthesis (or the second term in the right-hand side of Equation (12)) arises from the variation of the Lorentz factor, i.e., due to the relativistic effect. In the nonrelativistic limit, therefore, Equation (16) represents a trapping motion in the perpendicular momentum space with frequency $\omega_{\mathrm{trap}} = b_w v_{\mathrm{ph}}/u_0 = (B_w/B_0)(\omega/kc)(1/u_0)$. However, in the relativistic case with $b_w v_{\mathrm{ph}}\gamma_0^3/u_0^3 < 1$, $\delta u_\perp$ (and $\delta\psi$) diverges in time. When u_0 is small enough so that $\gamma_0 \approx 1$, the above inequality is hardly satisfied. In such a case, the fixed point is stable. But if u_0 becomes large and the inequality is satisfied, such an electron gains transverse energy while it keeps being trapped in the x-direction. We consider this solution later more in detail.

For the fixed point II, equations corresponding to Equations (15) and (16) are obtained by formally changing the sign of b_w. Therefore, the system is unstable for parallel fluctuations while it is stable for perpendicular fluctuations. This fixed point is actually conjugate to the relativistic fixed point discussed above. Another fixed point (III), conjugate to the nonrelativistic one, which should be a saddle point in $u_\perp - \psi$ phase space, appears at $(u_\perp, \psi) = (0, n\pi)$ as singular points of $du_\perp/d\psi$, where $n = 0, \pm1, \pm2, \ldots$.

3.3.2. Features in $u_\perp - \psi$ Phase Space

In order to study perpendicular dynamics, let us first consider a reduced system in which parallel quantities are fixed at the fixed point, i.e., $u_\parallel = 0$ and $\kappa\xi = \pi/2$. Then we only have to consider the following two equations:

$$\dot{p} = 2\sqrt{p}\, b_w v_{\mathrm{ph}}\cos\psi \tag{17}$$

$$\dot{\psi} = -\frac{b_w}{\sqrt{p}} v_{\mathrm{ph}}\sin\psi - \left(\nu - \frac{1}{\sqrt{1+p}}\right). \tag{18}$$

Here, $p = u_\perp^2$ has been introduced. This system has a Hamiltonian defined as

$$H(p, \psi) = 2\sqrt{p}\, b_w v_{\mathrm{ph}}\sin\psi + \nu p - 2\sqrt{1+p}, \tag{19}$$

where $\dot{p} = \partial H/\partial\psi$ and $\dot{\psi} = -\partial H/\partial p$ are satisfied. Contours of the Hamiltonian for $b_w = 1.0$, $v_{\mathrm{ph}} = 0.17$, and $\nu = 0.11$ are represented as gray lines of the upper (linear scale) and lower (logarithmic scale) panels in Figure 5(a). The above parameters are chosen so that the waves interacting with the accelerated electron in the second acceleration stage observed in the PIC simulation (Figure 3(e)) is appropriately reproduced. It is easily confirmed that a center at $\psi = \pi/2$, which is clearly recognized in the lower panel, corresponds to the nonrelativistic stable fixed point of the fixed point I and another center at $\psi = 3\pi/2$, which can be seen both in the upper and lower panels, to the relativistic fixed point II discussed above.

The nonrelativistic center should satisfy the following condition from Table 1:

$$-\frac{b_w v_{\mathrm{ph}}}{u_0} = \nu - \frac{1}{\gamma_0}. \tag{20}$$

Although $\nu - 1/\gamma_0 = 0$ in the small amplitude limit, it is never satisfied in the nonrelativistic case since $\nu < 1$. Therefore, the nonrelativistic center appears only when the wave amplitude becomes finite. The closed trajectories around this center essentially coincides with the nonresonant trapping discussed by Kuramitsu & Krasnoselskikh (2005).

At the relativistic center, the resonance condition $\nu - 1/\gamma_0 = 0$ should be satisfied in the ultrarelativistic limit, since $b_w v_{\mathrm{ph}}/u_0$ is negligible. In such a case, relativistic decrease of the gyro frequency allows another resonance with low-frequency waves. This resonance can also be present in a small-amplitude limit. Relativistic linear resonance conditions between an electron and two oppositely propagating waves ($\gamma\nu \mp \kappa u_\parallel - 1 = 0$) are shown in Figure 5(c). The two resonance lines intersect at $u_\parallel = 0$ where $\nu - 1/\gamma = 0$ and $\gamma = \sqrt{1 + u_\perp^2}$ are satisfied, while there never appears such an intersection in the nonrelativistic limit. This indicates that an electron can resonate simultaneously with two waves in the relativistic case. By using Equation (19), the maximum width of the separatrix in $u_\perp$ is estimated as

$$\Delta u_\perp = 4\sqrt{\frac{b_w}{\kappa\nu}}. \tag{21}$$

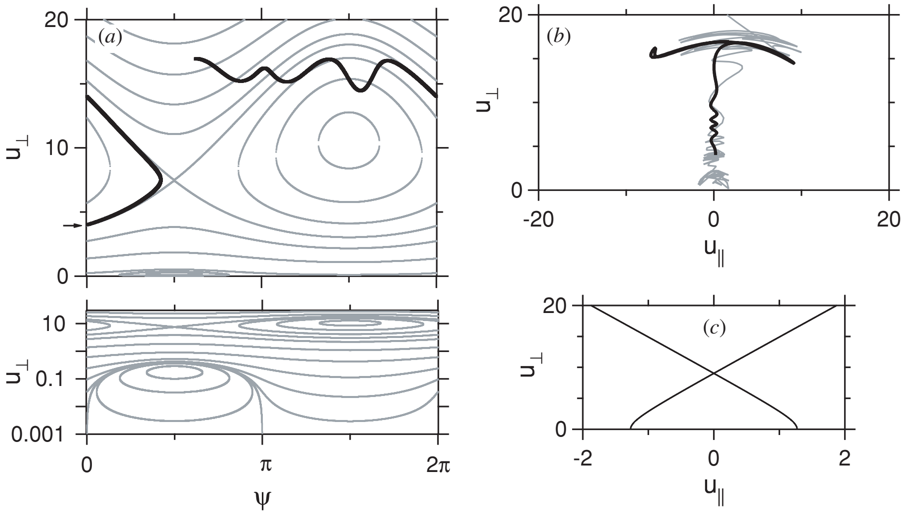

Figure 5. Electron trajectories in (*a*) $u_\perp - \psi$, (*b*) $u_\perp - u_\parallel$ phase space, and (*c*) linear resonance conditions of wave–particle interactions in a relativistic plasma. Solutions of Equation (19) are plotted as gray lines in (*a*). In (*b*), the gray line denotes a trajectory of the electron shown in Figure 3. A numerical solution of Equations (5)–(8) for $\Omega_w/\Omega_0 = 1$, $kc/|\Omega_0| = 0.65$, and $\omega/|\Omega_0| = 0.11$ is indicated as black lines in (*a*) and (*b*).

Furthermore, the maximum $u_\perp$ on the separatrix is given by

$$u_{\perp,\max} = \left(\sqrt{\frac{b_w}{\kappa}} + \sqrt{\frac{1}{\nu}}\right)^2 = \left(\sqrt{\frac{B_w}{B_0}\frac{\Omega_0}{kc}} + \sqrt{\frac{\Omega_0}{\omega}}\right)^2. \quad (22)$$

For instance, $u_{\perp,\max} \approx 18.4$ for the parameters used in Figure 5. This gives a good agreement with the electron energy achieved in the end of the second acceleration stage observed in the PIC simulation.

So far we have only looked at a subset of the system in which $\delta u_\parallel = 0$. If we allow $\delta u_\parallel$ to slightly deviated from zero, it should satisfy

$$\delta \ddot{u}_\parallel = -b_w \frac{u_0}{\gamma_0^2} \kappa \sin\psi \, \delta u_\parallel \quad (23)$$

around the fixed point in the original system Equations (5)–(8). Hence, the system is stable for $0 < \psi < \pi$ and is unstable for $\pi < \psi < 2\pi$ in terms of parallel fluctuations. The black solid line in Figures 5(a) and (b) shows a numerical solution of Equations (5)–(8). A trajectory of the electron initially positioned near the separatrix at $\psi = 0$ (indicated by a small arrow in Figure 5(a)) is represented. The electron moves almost along the separatrix when it is in $0 < \psi (< \pi)$. But when the electron enters in $\pi < \psi < 2\pi$, its trajectory starts deviating from the separatrix. And finally it is clearly detrapped when it approaches $\psi = 3\pi/2$. The trajectory in the momentum space shown in Figure 5(b) is very similar to what is observed in the PIC simulation which is again plotted as a gray line.

3.4. Statistics of High-Energy Particles

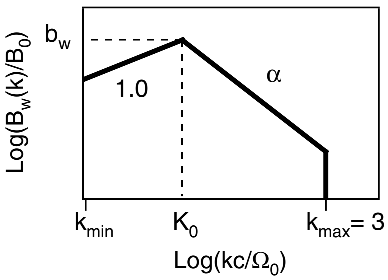

Figure 6. Wave power spectrum used in the test particle simulation.

Let us briefly discuss the power-law-like distribution of electrons in the current acceleration process. It is shown in Figure 2(a) that a high-energy tail with a power-law index ~ -2.5 evolves in the late stage of the simulation. This power-law nature may be related to the power-law spectrum of the wave amplitude of magnetic fluctuations. In the stage of successive decay instabilities ($\Omega_0 t > 100$), a spectral cascade of the magnetic fluctuations occurs with keeping a power-law index of the wave amplitudes almost constant with ~ -2.0 (Figure 2(b)). The enhancement of the wave amplitude at a higher wavenumber regime, $kc/\Omega_0 > 3$, is the remnant of initial parent wave and side band waves generated by the modulational instabilities in the early stage of the run. In order to confirm correlations between the wave and electron energy spectra, the following test particle simulation with periodic boundary conditions is performed. Waves are given by superposition of a number of right-hand-polarized Alfvén waves with the power-law spectrum shown in Figure 6 (the power-law index α is an external parameter), which models the lower wavenumber part of Figure 2(b). Both positive and negative wavenumber modes are evenly distributed. The wave form is given by

$$\begin{pmatrix} B_y \\ B_z \end{pmatrix} = \sum_{kc/\Omega_0=-3}^{3} b_w B_0 \left|\frac{k}{K_0}\right|^\alpha \begin{pmatrix} \sin(k(x - v_{\mathrm{ph}}t) + \Phi_k) \\ \cos(k(x - v_{\mathrm{ph}}t) + \Phi_k) \end{pmatrix}, \quad (24)$$

where $v_{\mathrm{ph}}/c = 0.17$ and $\{\Phi_k\}$ are initial wave phases which are randomly distributed at $t = 0$, and corresponding transverse electric fields are given by $\mathbf{k} \times \mathbf{E} = (|k| v_{\mathrm{ph}}/c)\mathbf{B}$. The power-law index α is fixed to 1.0 for $k_{\min} \leqslant k \leqslant K_0$, where $k_{\min} \equiv 2\pi/L$ and K_0 is the coherence wavenumber. The system size $L = 80\pi c/\Omega_0$ is common for all the following runs, and $b_w = 0.75$ and $K_0 c/\Omega_0 = 0.1$ if not specified.

In such a system where a number of waves propagate in two opposite directions, the particles are expected to be stochastically accelerated via a second-order Fermi-like process. First, this is confirmed by solving nonrelativistic equations of motion of 10^5 electrons. An initial distribution function is given as a spatially homogeneous gyrotropic ring distribution with

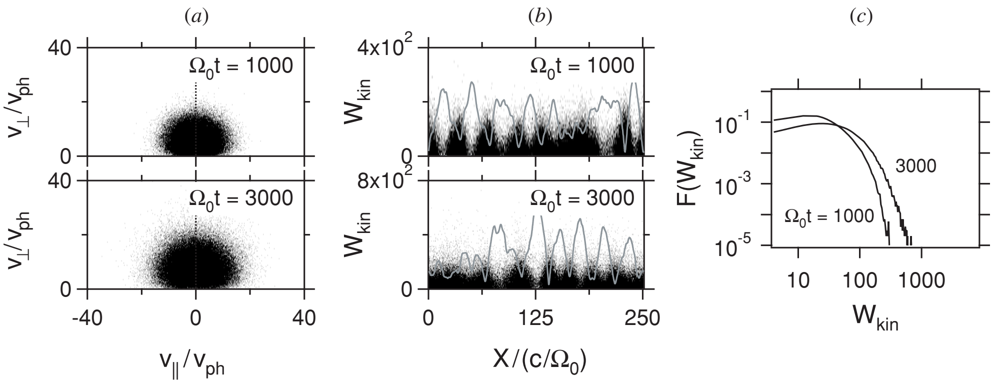

Figure 7. Results of nonrelativistic test particle simulation. Electron distributions in (*a*) $v_\perp - v_\parallel$ and (*b*) $X - W_{\rm kin}$ phase spaces, and (*c*) energy distribution functions at $\Omega_0 t = 1000$ and 3000, respectively. The solid gray lines in (*b*) denote profiles of magnetic field envelopes at the corresponding times.

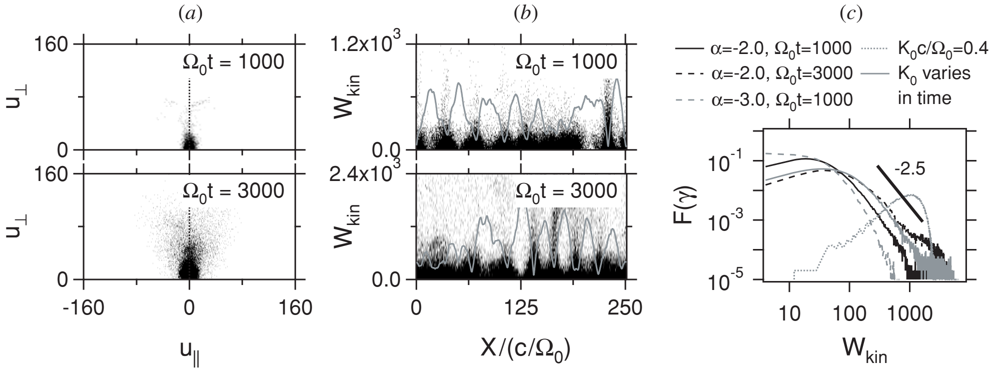

Figure 8. Results of relativistic test particle simulation in the same format as Figure 7. A number of energy distribution functions are plotted in (*c*). See details in the text.

$v_\perp/v_{\rm ph} = 0.1$. Figure 7 shows distributions in (a) $v_\perp - v_\parallel$ and (b) $X - W_{\rm kin}$ phase spaces, and (c) energy distribution functions at two different times, $\Omega_0 t = 1000$ and 3000, respectively, where $\mathbf{v} = (v_\parallel, v_\perp)$ denotes the particle velocity and $W_{\rm kin} = v^2/2v_{\rm ph}^2$ is the normalized kinetic energy. The solid gray lines in Figure 7(b) denote the envelope profiles of given magnetic fluctuations. The particles are spatially bunched around the troughs of the magnetic envelopes because of mirror effect. In the velocity space, the particles rapidly pitch angle diffuse (Figure 7(a)) while the averaged particle energy slowly increases in time (Figure 7(c)). These are the features of a stochastic or a second-order Fermi acceleration. In comparison, drastic changes occur if relativistic effects are taken into account. The simulation results with the same initial conditions as in the nonrelativistic case are plotted in Figure 8 with the same format as Figure 7. Here, the normalized kinetic energy is defined as $W_{\rm kin} = (\gamma - 1)c^2/v_{\rm ph}^2$. Compared with the nonrelativistic case, the maximum particle energies at each corresponding time are extremely higher, and they are at the same order as that obtained from Equation (22) with $k = K_0$ and $b_w = 0.75$ (the black solid and black dashed lines in Figure 8(c)). Spatial bunching of particles similar to the nonrelativistic case is found in Figure 8(b), while a fraction of the bunched particles are accelerated to extremely high energies. Such high-energy particles have rather large pitch angles, denoting perpendicular acceleration (Figure 8(a)). Interestingly, a power-law-like energy distribution appears only at $\Omega_0 t = 1000$ in Figure 8(c), although the corresponding energy range in the distribution function is small (the black solid line). The power-law index does not change even in the case with a different initial ring velocity, $v_\perp/v_{\rm ph} = 5.1$ (not shown). However, the spectrum becomes softer when $\alpha = -3.0$ is assumed (the gray dashed line in Figure 8(c)). When the coherence wavenumber is large as $K_0 c/\Omega_0 = 0.4$, the bulk electrons are accelerated and the energy distribution is no longer power law at $\Omega_0 t = 1000$ (the gray dotted line in Figure 8(c)). It is noted from Equations (21) and (22) that the minimum $u_\perp$ of the separatrix of the relativistic resonance of the dominant wave mode at $k = K_0$ decreases with increasing K_0. Hence, most of electrons which initially distribute below the separatrix can enter inside the separatrix through stochastic motions at a rather early stage, and they can be perpendicularly accelerated within a short time in the similar way seen in the previous section (see Figure 5). The peak energy is roughly consistent with the $u_{\perp,\rm max}(\sim 940)$ estimated by using $b_w = 0.75$ and $\kappa = 0.4$ from Equation (22). In contrast, for a small wave amplitude, $b_w = 0.1$, the maximum energy at $\Omega_0 t = 1000$ is much smaller than the value obtained from Equation (22) (not shown). The reason may be that in this run the minimum $u_\perp$ of the separatrix is rather high because of its narrow width so that particles which initially distribute far below the separatrix have not entered in it until this time.

In Figure 8(c), the power-law-like nature appears as a transient state in the system at $\Omega_0 t = 1000$ for $\alpha = -2.0$. In this run, at later time ($\Omega_0 t = 3000$), the high-energy end of the particle distribution is so enhanced that the energy distribution does not fit the power-law spectrum (black dashed line). It is confirmed that the hump of the high-energy part grows at least till $\Omega_0 t = 6000$. After sufficiently long time, it probably results in bulk acceleration as seen in the case of small K_0. In the PIC simulation, the wave spectrum is not

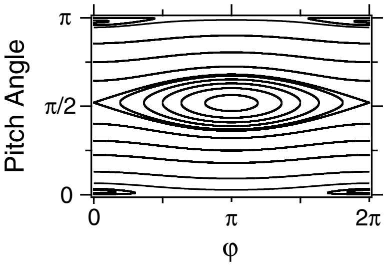

Figure 9. Trajectories of relativistic electrons interacting with the monochromatic circularly polarized parent wave. $B_w/B_0 = 1$, $kc/\Omega_0 = 6.21$, and $u = 0.64$ are assumed.

time stationary but cascading through the successive decay instabilities as already mentioned. In other words, a wave with a certain wavenumber has finite life time. This may be why the high-energy tail evolves without extra accumulation at the high-energy end of the distribution function in the late stage, $\Omega_0 t > 316$, of the PIC simulation (Figure 2(a)). To confirm this, an additional test particle simulation is performed by assuming that the wavenumber of the magnetic field with maximum intensity varies in time as $K_0 c/\Omega_0 \sim (\Omega_0 t)^{-0.9}$ which gives a reasonable fit in the late stage of the PIC simulation. The particle distribution and waves at $\Omega_0 t = 1000$ in the run corresponding to the black solid line in Figure 8(c) are chosen as initial conditions. Then, in the later time $\Omega_0 t = 3000$, the high-energy tail extends roughly obeying the power law and some low-energy particles remain unaccelerated, as shown in Figure 8(c) as the gray solid line.

4. SUMMARY AND DISCUSSIONS

In the present paper, an efficient particle acceleration process in the course of successive parametric instabilities of large-amplitude Alfvén waves was investigated. The acceleration takes place as a result of interactions between coherent waves in the developing Alfvén turbulence and relativistic particles. An important point is that relativistic wave–particle interactions allow simultaneous resonance between a particle and two different waves. The maximum attainable energy through this acceleration process was analytically estimated.

In this acceleration process, a high-energy particle is preferentially accelerated. During the successive decay instabilities, a peak of the wave Fourier spectrum shifts in time toward a lower-frequency (longer wavelength) regime. Because of relativistic decrease of particle's gyro frequency, low-frequency waves preferentially resonate with and accelerate particles with large energy. Therefore, if once a particle is accelerated and its effective mass is increased, in later time such a particle easily satisfies the resonance condition with lower-frequency waves generated by successive decay processes. Figure 3(a) shows an example of such an electron's energy time history in which one can recognize four acceleration phases around $\Omega_0 t \sim 170, 430, 1200,$ and 1550.

By utilizing test particle simulations in Section 4, it is shown that relativistic effects are essential in producing nonthermal particles. Note that the system discussed in Section 3 is exactly the same as that discussed by Wykes et al. (2001a, 2001b), although they mainly focused on stochastic off-resonance diffusion in the phase space with an application to planetary magnetospheres in mind. Actually, the regular trajectories in Figure 3(d) in Wykes et al. (2001a) correspond to the relativistic resonance focused in this paper. Enhancement of the Lyapunov exponent at $\omega \sim \Omega_0/n\gamma$, where n is an integer, shown in their Figure 8 might be related to the relativistic resonance. In our test particle simulation, the power-law-like energy distribution function similar to what was observed in the PIC simulation is reproduced by assuming the time-evolving Fourier spectrum of the Alfvén turbulence. The finite life time of a wave mode in developing the turbulence may contribute to the creation of such a distribution function. However, details of the acceleration process including the analytical estimate of the power-law index are still unclear and will be investigated in the near future.

The acceleration process discussed in this paper is essentially different from some of the recently studied coherent acceleration processes, i.e., electron surfing acceleration and wake field acceleration. In these processes, electrostatic field plays essential roles. Furthermore, the processes mainly affect electrons since generated electrostatic waves have rather high frequencies, while ion acceleration may also occur in a very late stage of nonlinear evolution of a system (Hoshino 2008). In the acceleration process discussed here, the roles of electrostatic fields are subdominant, although they are necessary for the decay instabilities. It should be noted further that the process may be able to act on ions too when a left-hand polarized wave is introduced as an initial parent wave. The Alfvén waves are essentially incompressible so that they may survive for a rather long period compared with electrostatic Langmuir or ion acoustic waves. Hence, the process may last for long time, and may also follow the above-mentioned electrostatic acceleration processes in some occasions.

In the present study, all the multidimensional effects have been excluded. In higher-dimensional cases, daughter waves propagating in oblique to the ambient magnetic field can also have finite growth rates (Viñas & Goldstein 1991). It is confirmed by MHD simulation that these waves destroy the planar structure assured in a one-dimensional simulation (Ghosh et al. 1993, 1994; Del Zanna et al. 2001). However, in a low-frequency regime, the decay instability of parallel propagation is dominant (Viñas & Goldstein 1991). Therefore, at least in such a regime the acceleration process observed here is expected to work, while the acceleration rate may decrease to some degree because of the appearance of nonplanar structures. This is similar to what is discussed for electron surfing acceleration in which the acceleration takes place even in two-dimensional cases despite the decrease in the acceleration rate (Amano & Hoshino 2009). At all events, further investigations are necessary for estimating the efficiency of this acceleration process in a more realistic situation.

We finally give a comment on applications of this acceleration process. Since the situation simulated in Section 2 is rather general, there may be several fields of application such as pulsar wind nebula, pulsar magnetosphere, outflow of GRB, and AGN jet, and so on. Vicinity of a relativistic shock is probably one of the candidates. Similar to the earth's foreshock, large-amplitude Alfvén waves may be generated by beam–plasma interactions between backstreaming ions and an upstream plasma, and the waves nonlinearly evolve via parametric instabilities. Since the acceleration is efficient and locally takes place, it may contribute to the so-called injection process into the DSA. As another possible case, cosmic ray–plasma interactions upstream of a supernova remnant shock are now extensively studied after the pioneering works by Lucek & Bell (2000), Bell & Lucek (2001), and Bell (2004, 2005). Most of such studies pay attention to the amplification of upstream magnetic fluctuations that can be scatterers of cosmic rays. And that is expected to result in the increase of maximum attainable energy in the DSA process. On the other hand, amplified magnetic fluctuations may lead to the local and the coherent acceleration processes discussed here. In other words, some particles may be accelerated through this process without crossing a shock. In this sense, the process is similar to the so-called second-order Fermi acceleration, although an efficiency of the acceleration process discussed here is much higher than that of the second-order Fermi process as shown by the test particle simulation.

The authors thank Victor Muñoz for useful discussions. The PIC simulation was performed by the super computer in ISAS/JAXA Sagamihara. This work was supported in part by Incentive Aid to the Prominent Research, Interdisciplinary Graduate School of Engineering Sciences, Kyushu University 2007.

APPENDIX

MOTION OF A RELATIVISTIC PARTICLE IN A MONOCHROMATIC WAVE

According to Kuramitsu & Krasnoselskikh (2005), an equation of motion of an electron in a monochromatic circularly polarized wave in a wave frame is reduced as

$$\dot{\mu} = -\frac{\partial H}{\partial \psi}, \qquad \dot{\psi} = \frac{\partial H}{\partial \mu}, \tag{A1}$$

where μ is the pitch angle cosine, ψ is the particle gyrophase with respect to the wave phase, and

$$H = \frac{K}{2}\left(\mu + \frac{1}{K}\right)^2 + b_w\sqrt{1-\mu^2}\cos\psi \tag{A2}$$

is the Hamiltonian. The above expressions are held even when relativistic effects are taken into account by putting $K = ukc/\Omega_0$ and $b_w = (B_w/B_0)\sqrt{1 - v_{\mathrm{ph}}^2/c^2}$. Electron trajectories interacting with the parent wave ($B_w/B_0 = 1$ and $kc/\Omega_0 = 6.21$) for different values of H are plotted in Figure 9. Here, $u = 0.64$ is assumed since the value is derived as average one at $\Omega_0 t = 70$ in the PIC simulation. The factor of v_{ph}^2/c^2 is neglected because of its smallness. Figure 9 is essentially the same as Figure 5 in Kuramitsu & Krasnoselskikh (2005). The maximum value of half the width of the separatrix is ~ 0.5 (at $\psi = \pi$), which roughly coincides with the standard deviation of the pitch angle observed in the PIC simulation at $\Omega_0 t = 70$ (Figure 2(c)).

REFERENCES

Amano, T., & Hoshino, M. 2007, ApJ, 661, 190
Amano, T., & Hoshino, M. 2009, ApJ, 690, 244
Axford, W., Leer, I. E., & Skadron, G. 1977, Proc. 15th Int. Cosmic Ray Conf. Plovdiv (Sophia: Bulgarian Academy of Sciences), 11, 132
Bell, A. R. 1978, MNRAS, 182, 147
Bell, A. R. 2004, MNRAS, 353, 550
Bell, A. R. 2005, MNRAS, 358, 181
Bell, A. R., & Lucek, S. G. 2001, MNRAS, 321, 433
Blandford, R. D., & Eichler, D. 1987, Phys. Rep., 154, 1
Blandford, R. D., & Ostriker, J. P. 1978, ApJ, 221, L29
Bruno, R., & Carbone, V. 2005, Living Rev. Solar Phys., 2, 4, http://www.livingreviews.org/lrsp-2005-4
Chin, Y. C., & Wentzel, D. G. 1972, Ap&SS, 16, 465
de Wit, T. D., Krasnosel'skikh, V. V., Dunlop, M., & Lühr, H. 1999, J. Geophys. Res., 104, 17079
Del Zanna, L., Velli, M., & Londrillo, P. 2001, A&A, 367, 705
Dieckmann, M. E., Eliasson, B., Parviainen, M., Shukla, P. K., & Ynnerman, A. 2005, MNRAS, 367, 865
Dieckmann, M. E., Eliasson, B., & Shukla, P. K. 2004, ApJ, 617, 1361
Drury, L. O'C. 1983, Rep. Prog. Phys., 46, 973
Duffy, P., & Blundell, K. M. 2005, Plasma Phys. Control. Fusion, 47, B667
Galeev, A. A., & Oraevskii, V. N. 1963, Sov. Phys. Dokl., 7, 988
Ghosh, S., Viñas, A. F., & Goldstein, M. L. 1993, J. Geophys. Res., 98, 15561
Ghosh, S., Viñas, A. F., & Goldstein, M. L. 1994, J. Geophys. Res., 99, 19289
Hada, T., Koga, D., & Yamamoto, E. 2003, Space Sci. Rev., 107, 463
Hada, T., Matsukiyo, S., & Muñoz, V. 2004, 12th Int'l Cong. Plasma Phys., 2004 October 25–29, Nice, arXiv:astro-ph/0410203
Hoshino, M. 2008, ApJ, 672, 940
Hoshino, M., & Shimada, N. 2002, ApJ, 572, 880
Jones, F. C., & Ellison, D. C. 1991, Space Sci. Rev., 58, 259
Katsouleas, T., & Dawson, J. M. 1983, IEEE Trans. Nucl. Sci., 30, 3241
Krymsky, G. F. 1977, Sov. Phys.-Dokl., 23, 327
Kuramitsu, Y., & Hada, T. 2000, Geophys. Res. Lett., 27, 629
Kuramitsu, Y., & Hada, T. 2008, Nonlin. Process. Geophys., 15, 265
Kuramitsu, Y., & Krasnoselskikh, V. 2005, A&A, 438, 391
Lagage, P. O., & Cesarsky, C. J. 1983, A&A, 125, 249
Lucek, S. G., & Bell, A. R. 2000, MNRAS, 314, 65
Lyubarsky, Y. 2006, ApJ, 652, L1297
Malkov, E., & Drury, L. O'C. 2001, Rep. Prog. Phys., 64, 429
Matsukiyo, S., & Hada, T. 2003, Phys. Rev. E, 67, 046406
McClements, K. G., Dieckmann, M. E., Ynnerman, A., Chapman, S. C., & Dendy, R. O. 2001, Phys. Rev. Lett., 87, 255002
Narita, Y., Glassmeier, K.-H., & Treumann, R. A. 2006, Phys. Rev. Lett., 97, 191101
Nariyuki, Y., & Hada, T. 2005, Earth, Planets, Space, 57, e9
Nariyuki, Y., & Hada, T. 2006, Nonlin. Proc. Geophys., 13, 425
Sagdeev, R. Z., & Galeev, A. A. 1969, Nonlinear Plasma Theory (New York: Benjamin)
Shimada, N., & Hoshino, M. 2000, ApJ, 543, L67
Skilling, J. 1975a, MNRAS, 172, 557
Skilling, J. 1975b, MNRAS, 173, 245
Skilling, J. 1975c, MNRAS, 173, 255
Spangler, S. R., & Fuselier, S. 1988, J. Geophys. Res., 93, 845
Spangler, S. R., Leckband, J. A., & Cairns, I. 1997, Phys. Plasmas, 4, 846
Tajima, T., & Dawson, J. M. 1979, Phys. Rev. Lett., 43, 267
Terasawa, T., Hoshino, M., Sakai, J. I., & Hada, T. 1986, J. Geophys. Res., 91, 4171
Viñas, A. F., & Goldstein, M. L. 1991, J. Plasma Phys., 46, 129
Wentzel, D. G. 1974, ARA&A, 12, 71
Wykes, W. J., Chapman, S. C., & Rowlands, G. 2001a, Planet. Space Sci., 49, 395
Wykes, W. J., Chapman, S. C., & Rowlands, G. 2001b, Phys. Plasmas, 8, 2953